Imaging of Individual Polymers Undergoing Flow in a Bed of Small Spheres

Chad D. DeLong and David A. Hoagland*

Department of Polymer Science and Engineering, University of Massachusetts Amherst, Amherst, Massachusetts 01003

Received February 26, 2008; Revised Manuscript Received April 13, 2008

ABSTRACT: Flexible DNA molecules are imaged by fluorescence microscopy while undergoing convection through micron-sized pores of a packed sphere bed. To circumvent the high pressures of a closed channel design, an open channel microfluidic device is selected such that sphere wicking drives convection. Image analysis yields the average level of chain stretching and the average DNA migration rate as a function of Deborah number *De* for ratios of sphere diameter to coil radius of gyration of order 1 to 10. Visualizations also reveal the transient localized conformations and trajectories of individual molecules, which can migrate only by traversing coil-sized pore constrictions. Two *De* (flow) transitions are noted: the first, at $De \sim 0.3$, leads to limited chain stretching, while the second, at $De \sim 1$, leads to gross chain stretching via a mechanism of entanglement about sphere contact points. Entangled chains adopt elongated "U"- and "J"-shaped conformations, which are relaxed by "pulley-like" sliding over entanglement points. Entanglement onset is associated with increase in average DNA migration rate, which abruptly shifts from below to above that for solvent. Results are discussed in the context of visualization results from gel electrophoresis and implications for polymer chromatography.

Introduction

Chromatographic techniques separate synthetic polymers by molecular weight or molecular architecture during polymer convection through a porous medium; examples include gel permeation chromatography,[1,2] hydrodynamic chromatography,[3,4] and slalom chromatography,[5,6] each accomplishing separation through slightly different polymer-flow-confinement dynamics. Although extensively probed via macroscopic measurements, specifically of polymer migration rate[3–6] and excess pressure drop,[7] these dynamics have not yet been microscopically visualized. For electrophoresis in gels, on the other hand, where the swollen cross-linked network can be considered a tenuous porous medium, visualization of individual chain dynamics has afforded significant insights into separation mechanisms.[8,9] Most synthetic polymers are uncharged and insoluble in water, mandating a chromatographic rather than an electrophoretic approach to separation. For large polymers, visualization by fluorescence microscopy has the potential to reveal chain configurations and chain locations across representative pore spaces at a time resolution of order 50 ms and a spatial resolution of order 0.2 μm. In this paper, visualization is reported for individual, flexible DNA molecules flowing in a packed bed of micron-sized impenetrable spheres, an environment in which the molecules separate by both molecular weight and molecular architecture. Since the spheres of the bed are not much larger than the mobile DNA molecules, pore constrictions of coil dimensions must be overcome to accomplish DNA flow migration. Chain conformation and chain migration rate in this complex environment are strongly affected by average fluid velocity. The dynamics described here have relevance to molecular topology fractionation (MTF), a newly discovered chromatographic means for separating synthetic polymers by architecture.[10]

The first visualization of polymers in flow was by Chu and Perkins,[11] who monitored the conformations of large, flexible DNA molecules near/at the stagnation point of a steady elongational flow. The molecules were observed to stretch above a critical Deborah number *De*, confirming earlier polymer flow birefringence and light scattering studies.[12] Less expectedly, incoming conformation was found by visualization to exert a strong influence on a molecule's subsequent stretching, with kinked- and dumbbell-shaped conformations extended most fully.[11] More recently, DNA molecules were visualized in additional model flows,[13–15] including flow through a sparse array of posts.[16]

Microscopically, porous media flows resemble the elongational flows of Chu and Perkins, and in particular, as molecules are convected through a packed bed of particles at high velocity, they repeatedly experience strong transient elongational flow stresses during passage through interparticle constrictions. However, flow is not Lagrangian steady and shear accompanies elongation/compression, with the different flow components mixed to differing extent at different pore locations. Consequently, stress histories experienced by individual chains are highly nonuniform. Recognizing dominance of the elongational flow component to polymer conformation, Haas et al.[17] characterized packed-sphere flows through a Deborah number *De*, defined—as for steady elongational flow—by the product of an elongation rate $\dot{\varepsilon}$ and the longest polymer relaxation time τ. Because of the flow's heterogeneity and unsteadiness, $\dot{\varepsilon}$ cannot be unambiguously specified: Haas et al. equated

$$\dot{\varepsilon} = k\left(\frac{\bar{v}}{d}\right) \tag{1}$$

where $\bar{v}$ is the superficial velocity and d is the sphere diameter. The prefactor k was argued on geometric grounds to adopt a value of $\sim$6,[17,18] reflecting the maximum of $\dot{\varepsilon}$ in the convergence created between three touching spheres. With this choice, onset of chain deformation, inferred by a jump of excess pressure drop, was correlated with an order unity critical value of *De*,[7] consistent with predictions for flexible polymer chains in steady, homogeneous elongational flow. Values of τ can be obtained from experiment or approximated from theory using the Zimm formula[19]

$$\tau = \frac{4.22\eta_s[\eta]M}{RT} \tag{2}$$

where η_s is the solvent viscosity, $[\eta]$ is the intrinsic viscosity, M is the polymer's molecular weight, R is the gas constant, and T is temperature.

Starting with Austin et al., the electric-field-driven migration of charged DNA has been visualized in various obstacle

* Corresponding author.

10.1021/ma800430a CCC: $40.75
Published on Web 06/03/2008

environments.[20–27] Ease of labeling with intercalating fluorescent dye and a stiff backbone make double-stranded DNA an ideal polymer for visualization studies. The first of these properties enables long-term observation of isolated, single chains, while the second expands kilobasepair or greater DNA chains into configurations larger than the diffraction limit of light (~0.2 μm). During gel electrophoresis under an applied electric field of increasing strength, configurational interactions with gel obstacles ("fibers") generate a sequence of prototypical DNA conformations.[8,9] At low fields, chains remain relaxed and spherically compact, but at large fields, collisions create transient "U"- and "J"-shaped conformations characterized by substantial stretching/orientation. Movies of chain motion at high field show flexible DNA molecules sequentially colliding with an obstacle, unraveling into "U" or "J" conformations that drape across the obstacle, "unhooking" by slow, pulley-like sliding around the obstacle, and eventual recovery of the unstretched conformation during subsequent, nearly free electrophoretic migration.[28,29]

For identical pore geometries, one might suppose that a scaling of field magnitudes could map the dynamics of electric-field-driven DNA motions onto the analogous flow-driven DNA motions. However, interactions of a charged polymer with an electric field are not the same as interactions with a flow field. For example, during motion in a uniform electric field, hydrodynamic interactions between distant chains segments are suppressed by dissociated counterions, while during flow-driven motion, they are not.[30] As a consequence, the relevant chain friction coefficients are unequal, even in their dependence on molecular weight. Further, the velocity gradient for flow within a pore manifests a no slip boundary condition at the wall, while the electric field gradient manifests a dielectric mismatch at the wall. Notwithstanding such distinctions, with increased field magnitude, migrating chains in the two cases might well experience a similar sequence of prototypical conformational states, a possibility discussed here as well as in Teclemariam et al.[16]

During gel electrophoresis, the cross section of gel obstacles is usually smaller than the average coil size of the migrating flexible molecule, and the dimensionless field magnitude is typically large; under these conditions, an obstacle can transiently "pin" a flexible molecule, and the molecule's distant sections will be stretched downfield until the pinning is relieved. Collision with an obstacle can thereby be viewed as a transient entanglement. The steric interaction of a convected flexible polymer in a bed of spheres, as envisaged by Haas et al. and others, is much different: stretching emanates from repeated imposition of gross hydrodynamic stresses on a flexible molecule flowing through converging pores. These dynamical differences manifest presumption of different particle-to-polymer size ratios, d/R_g. In the traditional description of packed bed or chromatographic flow, a migrating polymer is viewed as small compared to particle size ($d/R_g \gg 1$), excluding entanglement. In MTF, where particles are much smaller than in usual chromatography ($d/R_g \sim 1-10$), it is difficult to judge a priori which dynamics dominates: flow-induced "squeezing" between obstacles or flow-induced "entanglement" around them (or their contact points).[10]

The preceding discussion suggests that polymer solution flow in a packed bed of spheres should be governed by two reduced parameters, De and d/R_g. Additional parameters could emerge should the polymer's persistence length or excluded volume become important; however, we suspect only secondary impacts under the good solvent conditions typical of polymer chromatography. A long-term goal of the current project is to visualize linear DNA molecules as De and d/R_g vary, monitoring average migration rate and stretching level for each parameter combination, a procedure delivering a "map" of polymer dynamics for model porous media flows. In the current contribution, we establish conditions for this study, presenting the first visualization of polymers migrating in a pressured-driven packed bed (or chromatographic) flow. One key accomplishment is a simple means to circumvent the large pressure drops of nano- or microscopic pressure-driven flows. For water, at an average fluid velocity of 1 cm/min, the pressure drop across 1 cm of a 1 μm diameter cylindrical pore would be 0.5 atm, exceeding mechanical tolerances of the glass coverslips needed in optical microscopy. As described here, an open channel microfluidic flow eliminates this problem. Another important accomplishment is confirmation that conventional microscope optics can "see" far enough into an optically heterogeneous matrix, i.e., a bed of solvent-immersed spheres, to probe polymers in a porous medium flow little disturbed by the medium's external boundaries. A high magnification water-immersion microscope objective with long working distance enables clear imaging of molecules several microns inside a bed of immersed spheres even when the refractive indices of spheres and solvent do not match.

Work by Liu et al.[31,32] and Meunier et al.[10] render a porous media visualization study timely, as both groups recently studied chromatography of flexible polymers undergoing elution at relatively high velocity in packed beds of impenetrable spheres. Results of the two studies naively appear dissimilar: as reported by Liu et al., an increase of flow rate causes an increase in the retention times of high molecular weight polymers, while as reported by Meunier et al., an increase of flow rate causes a decrease in the retention time. The most obvious difference between experiments is d/R_g, large for Liu et al. and small for Meunier et al. These divergent outcomes illustrate the paramount significance of microscopic dynamics to chromatography, and molecular visualization is potentially the only direct way to assess these dynamics.

Experiment

Glass Coverslips. Open channel microfluidic flow devices were constructed on ordinary 0.13−0.17 mm thick glass coverslips previously printed with a hydrophobic/hydrophilic surface pattern by optical photolithography. To accomplish the patterning, a positive photoresist (SPR 220-7, Rohm and Haas) was spun onto a clean coverslip at 5400 rpm for 90 s. The coating was baked at 80 °C for 60 s before exposure through a mask to UV light (intensity = 20 MW/cm^2 and λ = 365 nm) for 100 s; the mask was an ordinary transparency onto which an appropriate pattern had been produced by an ink-jet printer. After a second 60 s bake, the exposed photoresist was removed with developer (MF-319, Rohm and Haas). UV-ozone treatment for 300 s (UVO-Cleaner, Jelight Co. Inc.) ensured complete oxidation of the exposed region, which was made hydrophobic by overnight exposure at reduced pressure to *n*-octyltrichlorosilane (TCI America) vapor at 70 °C. Unreacted silane and residual photoresist were removed with ethyl acetate. The patterned surface was finally washed with a solution of 1% Alconox detergent solution to remove trace organics. Figure 1A presents a sketch of the hydrophobic/hydrophilic pattern of optimized shape. During a visualization experiment, the circular hydrophilic pad at the top (diameter 0.5 cm) supported a buffer reservoir, while the elongated hydrophilic ellipse at the bottom (length 1.5 cm) hosted a test section of the particle bed.

Latex Particle Deposition. Nearly monodisperse 7 μm polystyrene latex particles (Fluka) were solution-cast (2% v/v) from water onto the hydrophilic portion of the patterned coverslip (spheres do not stick elsewhere), and the cast layer was allowed to dry in open air. Figure 1B shows a typical sphere packing as viewed through the underlying coverslip. Packing irregularities are comparable to those of a typical chromatography column; evaporation precluded long-range sphere ordering. Coatings were 3−5 particle diameters deep except near the hydrophobic/hydrophilic boundary, where packing depths were somewhat greater. In a few experiments, analogous but smaller 1.3 μm polystyrene latex spheres (Duke

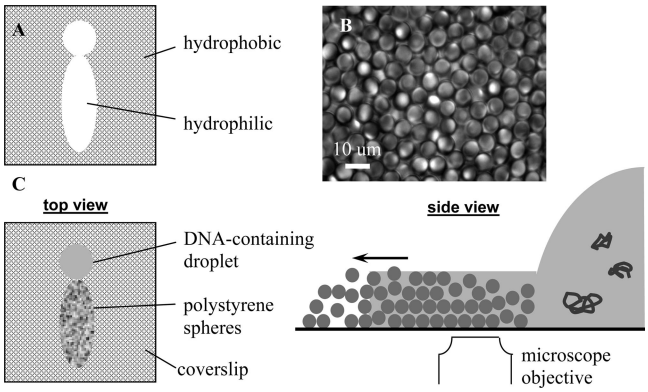

Figure 1. (A) Surface pattern for controlling droplet spreading and directionalizing wicking flow. (B) Typical packing achieved by solution casting of 7 μm polystyrene particles. (C) Top and side view of wicking flow device.

Scientific) were used in place of the larger bed particles.

Solutions. Into 1x TAE buffer, λ-DNA (New England Biolabs) was dissolved at 0.05 μg/mL along with sufficient TOTO dye (Molecular Probes) to establish a 4:1 ratio of basepair to dye. This solution was further modified with 25% (v/v) ethylene glycol and 10 mM sodium chloride, raising the viscosity to 1.6 cP. Carboxylate-modified fluorescent microspheres (0.1 μm, blue fluorescence (350 nm/440 nm) FluoSpheres, Molecular Probes) were employed as tracers to assess the instantaneous mean solvent velocity across the region imaged in the microscope. The supplier's stock dispersion was first sonicated, then centrifuged to remove aggregates, and finally diluted to a concentration of 6.3 pM (particles per volume) in the TAE buffer solution containing DNA, ethylene glycol, and sodium chloride. To verify that the microspheres were small enough to track solvent velocity accurately, a second set of flow experiments was performed in similar fashion with somewhat smaller microspheres (0.04 μm, yellow-green fluorescence (505 nm/515 nm), streptavidin-coated FluoSpheres, Molecular Probes), with no change in average velocity discerned.

Fluorescence Microscopy. To gather fluorescent images, a Zeiss inverted microscope fitted with a 63× water-immersion, C-Apochromat Zeiss lens with a 1.2 numerical aperture was used in conjunction with a Sensicam QE CCD camera (Cooke) operated under IPLab software (BD Biosciences). A 2× optical doubling lens in the downfield optical train magnified the image across the full camera surface. For an aqueous sample, the nominal working distance of the objective lens was 70 μm. Illumination for fluorescent imaging was provided by a 100 W mercury arc lamp (Zeiss HBO 100 AttoArc); 470 nm/515 nm (excitation/emission) filters were selected for viewing DNA, and 350 nm/420 nm filters were selected for viewing 0.1 μm microspheres.

Microfluidic Flow. A small volume of buffer solution (~4−5 μL) was deposited by micropipet onto the circular (reservoir) region of the patterned coverslip and allowed to wet the latex particles in this region for ~5 min. An experiment was stopped immediately if the droplet spread over particle bed outside the reservoir region. After 5 min of equilibration in the reservoir region (with incipient wicking into the particle bed), 2 μL of DNA solution and 2 μL of tracer solution were gently added to the droplet. The microscope objective, positioned about 0.5 cm downfield of the buffer reservoir, was sequentially focused on planes 0, 1, or 2 particle layers deep from the coverslip surface and left at this focus position for the remaining experimental period. The overall microscope-flow setup is shown in Figure 1C. DNA molecules were imaged with an exposure time of 100 ms at a frame rate of ~6/s. After changing the emission/excitation filter set, requiring a few seconds, tracers in the same bed region were imaged with an exposure time of 25 ms at a frame rate of ~13/s. A single bright-field still image of the particle packing was taken to accompany fluorescent image sequences.

Image Processing/Data Analysis. Image processing and data analysis were both executed using Image J software (NIH). Tracer images were collected immediately before/after DNA image sequences so as to obtain the near simultaneous average fluid velocity. This velocity changed but only over much longer times than required for the back-and-forth imaging procedure. DNA extension in the flow direction was equated to the full axial pixel spread defining a DNA molecule; no effort was made to correct for optical artifacts that slightly expand visualized size. These artifacts include finite optical resolution (diminished from that in a fully transparent medium) and finite frame rate (chain motion during image collection). For both DNA and tracer velocity measurements, a time-weighted average for center-of-mass displacement was chosen; for example, the "velocity" assigned to a molecule/tracer in the field of view for 17 frames was weighted by a factor of 16. [For DNA extension measurements, made without tracers for optimal image clarity, average fluid velocity was back-calculated from average DNA velocity.] All reported errors correspond to the error of the mean calculated from the number of observations and the measured distribution of the quantity of interest.

Results and Discussion

Microfluidic Flow Device. Because of their negative surface charge, the deposited hydrophilic bed particles are fully wetted by aqueous buffer, and capillary wetting drives the porous media flow. Nonetheless, the particles adhere to each other and the coverslip so strongly that their positions are not disturbed by flow. The microfluidic device thereby defines a flow environment analogous to that of thin layer chromatography. However, since the flow is horizontal and proceeds from a compact central fluid source, surface patterning is necessary to achieve unidirectional flow and prevent overspreading of the test bed section by the fluid reservoir. The neck between reservoir and test section achieves the latter task, fixing in place the reservoir droplet. Because of the test section's elongated elliptical shape, the wicking front widens only gradually after it progresses beyond the neck, minimizing flow entrance effects and eliminating unwet corner zones. While other patterns functioned almost as well, the pattern of Figure 1A was chosen from an array of similar test patterns for the ease of packing latex particles to almost uniform bed depth. After rinsing and drying, flow devices could be reused.

Fluid velocity varied with position of the wicking front and, in conformance with the Washburn equation for wicking flow, decreased approximately as the square root of time.[33] The front typically reached the imaging region in several minutes, and over subsequent individual image acquisition periods, the velocity reduction was minor (less than 10% of the average measured velocity). Several imaging periods, of 15 s duration, were spaced within a wicking run's overall 30−60 min time window; this window closed when the front either destabilized (i.e., became nonuniform) or stalled due to evaporation. Slight background fluorescence from the polystyrene latex particles was noted, and DNA chains occasionally degraded before or during viewing; neither effect impacted significantly the visualizing of DNA dynamics. Degradation led to DNA fragments readily identified by their smaller size. At higher *De*, strongly elongated chains sometimes broke under hydrodynamic stress, as confirmed by conformational recoil of the ensuing, nearly equal-sized fragments. More often, as observed at all *De*, light-induced degradation created a population of polydisperse fragments. The intercalating dye is responsible for this light sensitivity.

Choice of an open channel, wicking-driven flow device followed repeated failures to construct a closed channel, pressure-driven flow device allowing for fluorescence imaging; pumping a fluid through a particle-filled microchannel faced with a coverslip inevitably led to device overpressurization and

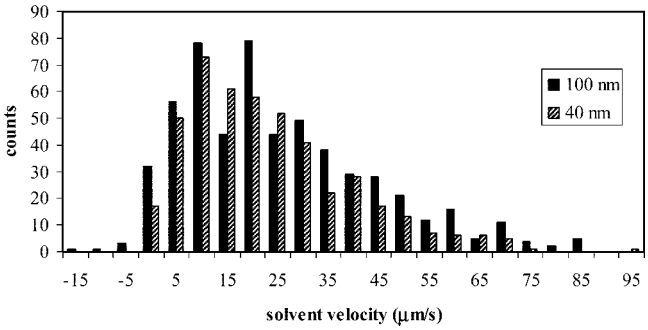

Figure 2. Histogram of velocities for tracers of different size.

mechanical failure. A penalty accompanies selection of an open channel design: loss of readily adjusted, steady fluid velocity. Inspection of governing equations shows that the material and geometric variables affecting velocity of a one-dimensional wicking flow are viscosity, air−fluid interfacial tension, fluid−particle interfacial tension, and particle size. None can conveniently be exploited to tune *De* while leaving constant d/R_g. For example, increasing viscosity reduces velocity, but since τ is proportionately to viscosity, *De* remains constant. Ethylene glycol was added to viscosify the buffer solely for the purpose of slowing polymer dynamics to time scales at which they can readily be captured (at the single polymer level) by the CCD camera.

The open channel design thus points to variation of *De* through dependence of the average fluid velocity on time. While this strategy worked well under most conditions, at the large times necessary to achieve *De* less than unity, the wicking front inevitably stalled due to evaporation. To circumvent the difficulty, a localized heat source (a hot plate at 100 °C) was applied briefly to the underside of the coverslip across a region downfield from visualization. This treatment caused a mild sintering of latex particles, which reduced the bed's permeability. When the wicking front entered the sintered region, fluid velocity upstream dropped, enabling microscopic measurements down to *De* of order 0.10.

At a bin size of 5 μm/s, Figure 2 shows velocity histograms for both 40 and 100 nm tracer particles. The histograms are similar, both displaying a maximum at ~15 μm/s and a tail extended to higher velocity. Note that, at the chosen flow condition, a few tracers move against the mean flow direction, and others reach 5 times the most probable velocity in the mean flow direction. For either tracer, the average velocity, as defined in the Experiment section, is around 30 μm/s. Since the two tracer results overlap to within experimental error, the subsequently quoted average velocity is always that for 100 nm tracers. Advantages of the 100 nm tracers were better brightness and an emission wavelength different from that of fluorescently stained DNA. We are unaware of any previous experimental or theoretical studies of microscopic velocity distributions for model porous media flows; it might be interesting to assign a functional form to these distributions or to compare them to distributions associated with other porous media flows.

At low average axial velocity, both Brownian motion and nonaxial localized velocity components caused tracers and DNA sporadically to move out of the focal plane, making conformations/trajectories difficult to follow across the full field of view. While excursions about the focal plane by about ±1 latex particle diameter lead to obvious defocus, molecule/particle position can still be unambiguously identified. Gathering frames at 50 ms intervals was sufficient to follow individual dilute chains or tracers for extended periods under all flow conditions tested (difficulty was greatest at lower velocities). The main

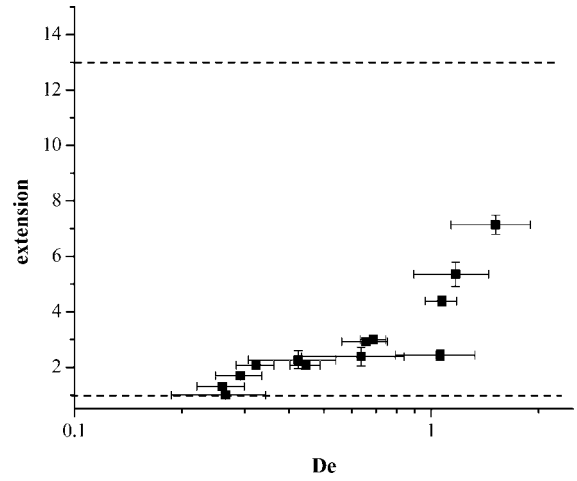

Figure 3. Normalized flow direction elongation (divided by quiescent image spread) plotted against Deborah number *De* for λ-DNA in 7 μm sphere bed. (Dotted lines indicate minimum and maximum elongation.)

chain properties gathered in this study, average chain extension and average migration velocity, are not impacted by out-of-plane motions except to the extent that these motions reduce the size of statistical samples. It is conceivable that a few chains extend and orient so that a portion of the molecule lies so far from the focal plane as to be "invisible". If so, chain extension might be underestimated. We believe such events to be extremely rare.

Average DNA Elongation. For $d = 7$ μm, Figure 3 plots the average flow-elongated dimension of λ-DNA as a function of *De*. The former parameter is normalized by the fluorescent molecule's measured span in absence of flow, and the latter is calculated using the Zimm formula for τ (yielding τ = 0.13 s).[19,34] While τ is changed by confinement, *De* here, and by most conventions, is defined by the slowest dynamics of the relaxed coil in a bulk quiescent solution. The figure's two dotted horizontal lines correspond to asymptotes of zero and full DNA stretching. As noted in the Experiment section, the reported coil size here corresponds to the full axial pixel spread of an imaged molecule. Without flow, this spread is 1−2 μm, which is larger than R_g (0.7 μm after dye intercalation[35]). The flow-elongated dimension in Figure 3 has been normalized by the axial spread of a molecule in absence of flow. The contour length of dye-intercalated λ-DNA is about 22 μm. However, because of the geometric constraints imposed by the packed bed (a fully stretched chain must zigzag around latex particles), the maximum achievable stretching is about 17 μm.

As expected, at $d/R_g = 10$, molecular extension grows with increasing *De*, displaying characteristic transitions. Surprisingly, there are two of these transitions. The first, at $De \approx 0.3$, initiates a prolonged *De* regime of limited DNA extension; while data near and below the onset are sparse, they are sufficient to demonstrate a transition that is gradual. Below the *De* transition, molecules fluctuate isotropically about their equilibrium rest conformation, hydrodynamic stretching barely perceptible. A typical conformation just above the transition is sketched in Figure 4A. Two features characterize stretching across this second regime: (i) extended chain dimensions are always less than 1−2 packing sphere diameters, and (ii) stretching accumulated during passage through one constriction substantially or completely relaxes over the time needed to reach a succeeding constriction. Migrating molecules do not necessarily stretch at every encountered constriction, and axial translations of 5−10 packing sphere distances are sometime incurred before a second stretching event. DNA conformation across this regime is thus

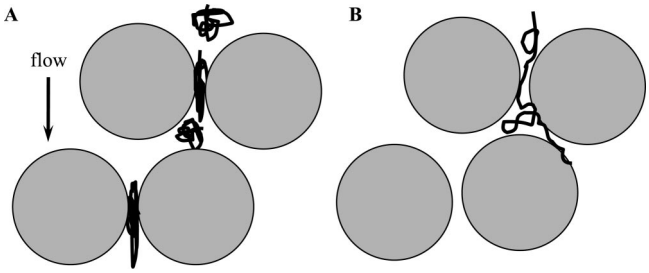

Figure 4. Prototypical λ-DNA deformation for (A) 0.3 < De < 1.0 and (B) *De* just above 1.0.

both limited in amplitude and highly transient. Molecules occasionally alternate repetitively between fast (stretched conformation) and slow (unstretched conformation) velocity states during passage through a series of pore constrictions and expansions.

The second, and much sharper, stretching transition occurs at $De \approx 1.0$. Above this transition, molecular extension, incomplete and unsteady to the highest *De* examined, is sustained. A depiction of one DNA conformation, typical of *De* barely above the transition, is given in Figure 4B. Axial stretching consistently exceeds 1−2 packing sphere diameters with intermittent relaxation rarely, if ever, complete. At *De* much above 1.0, as indicated in Figure 3, molecules reach substantial fractions of their uncoiled length. Indeed, at *De* of order 20, in experiments not fully reported because chain motion is too fast to allow unambiguous imaging of conformation, uncoiling appears complete for brief periods. At such high *De*, any uncoiled and aligned molecules adopt extended "sawtooth" configurations with their backbones zigzagging back and forth along a line of spheres oriented with the flow direction.

To quantify statistics of DNA stretching as a function of *De*, histograms of extension for several values of *De* are given in Figure 5; each histogram characterizes an entire set of imaged molecules for the given *De*. For the histogram gathered at $De = 0.30$, while most DNA molecules remain unstretched, a small fraction adopts slightly elongated or "blunted cigar" shapes. With *De* increased to 0.45, the overall average extension slightly grows, but most molecules remain essentially unstretched. The histogram is now more skewed toward its high side, indicating that stretched chains are somewhat more elongated than stretched chains at lower *De*. Raising *De* to 0.66 leads to two somewhat indistinct configurational populations: molecules that are almost unstretched, with extended lengths less than 2−4 μm (normalized extensions ≤2−3), and those that are moderately stretched, with extended lengths between 5 and 10 μm (dimensionless extensions ∼3−6). Finally, at $De = 1.1$, nearly all molecules are stretched, some to high degree (dimensionless extensions >5).

Many useful insights in DNA stretching emerge when viewing composite images that overlay a still image of the particle bed with a time-lapse sequence of DNA fluorescence images. Such composites reveal how localized chain stretching relates to localized bed structure. Figure 6A shows a region of the bed alongside images gathered at different times for a single traversing DNA molecule; flow is from bottom to top, and $De = 0.80$, just below the second transition. Figure 6B shows a magnified composite image constructed using the DNA configuration at 0.0 s. At this instant, the molecule loosely "winds" in an "S" shape about two neighboring spheres, its leading (topmost) "head" displaying slightly greater integrated intensity, a feature indicating segment accumulation in the relatively open void between four touching bed spheres. (Two of the spheres are in one vertical plane and the others are in the next, explaining the difference in apparent sphere size, intensity, and focus.) This

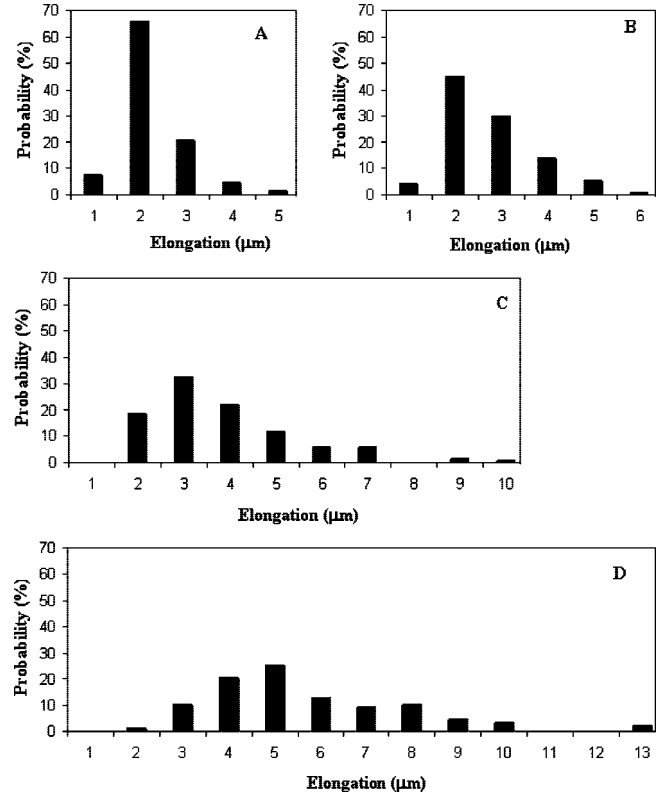

Figure 5. Histograms of DNA elongation for (A) $De = 0.3$, (B) $De = 0.45$, (C) $De = 0.66$, and (D) $De = 1.1$.

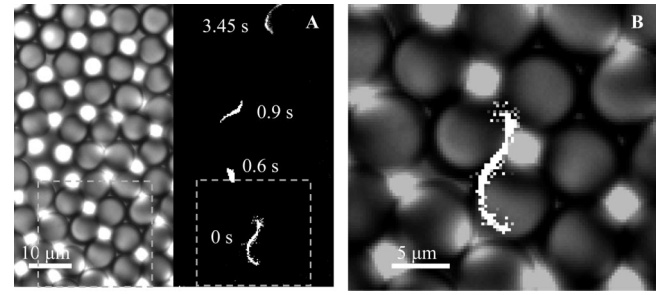

Figure 6. (A) Sphere packing (left) and corresponding time sequence of DNA conformations (right) for $De = 0.8$. Flow is from bottom to top. (B) Overlaid fluorescence and optical images showing DNA between particles at 0.0 s (dotted box in (A) indicates region displayed in (B)).

chain configuration is typical of stretched molecules across the regime $0.3 < De < 1.0$. Despite significant hydrodynamic stresses, configurational fluctuations (entropy) remain significant, as evidenced by the ability of the void to "reel in" the stretched segments that follow. At 0.6 s, the molecule, having moved downfield by 2−3 sphere diameters, is nearly relaxed to its quiescent size. Subsequent conformations show the molecule again stretched, not always in the direction parallel to the flow. At slightly higher *De*, just above the second transition, such a molecule never fully relaxes (as inferred here at 0.6 s) and extended sizes go beyond 1−2 sphere diameters. The trajectory traced by this molecule's center of mass roughly traces, but does not exactly track, the mean flow direction; deviations are attributed to translational Brownian motion, which is not totally overwhelmed at this flow conditions by convection. While traversing the field of view, this particular molecule always remained in focus.

Average DNA Migration Rate. Figure 7 shows the average axial velocity of λ-DNA vs *De*. Velocity here has been

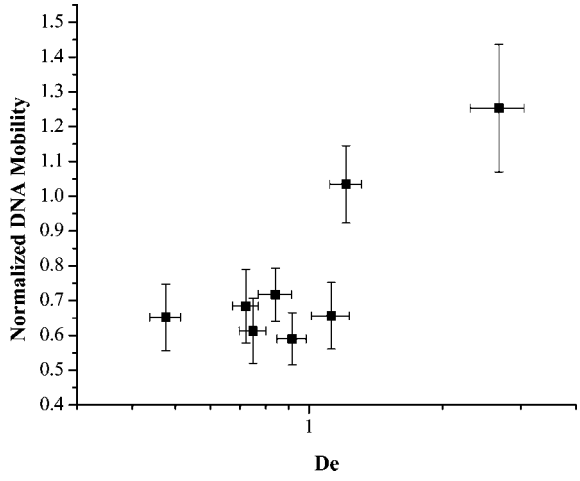

Figure 7. Normalized average DNA migration rate (divided by average solvent velocity) as a function of *De*.

normalized by the average velocity measured for small, neutral tracer particles, and so, the plotted variable should closely approximate the macroscopic retention factor measured during chromatography. At $De < 1.0$, DNA molecules move at a strongly hindered average rate that seems to be independent of De for a substantial range of *De*. Then, at *De* just above 1.0, the normalized DNA velocity rises abruptly, its value increasing from ~0.65 at $De = 0.3$ to ~1.2 at $De = 3.0$. Detailed trends in this higher *De* regime are not clear, as there are few data points and their errors are relatively large; most likely, a *De* plateau in normalized average velocity is not immediately achieved. At $De = 1.0$, a sharp decrease in the fraction of time spent in the coiled state, which has low mobility, appears to be the immediate cause of the velocity upturn. However, as described in the next section, the dynamics at higher De are much more complicated than this statement suggests. A connection between the second conformational transition and the average velocity transition is unequivocal.

Molecular Mechanisms of Extension/Hindered Motion. While average DNA extension and migration rate might be measured by nonmicroscopic means, microscopic visualization is unique in affording the time-dependent dynamics of individual DNA molecules, in essence, revealing how such molecules actually deform and move. Unfortunately, quantitative analysis of dynamical events by single molecule microscopy is difficult, so the following discussion of chain dynamics presents only qualitative observations and interpretations.

To migrate from a void between particles in a packed bed, a large, flexible DNA molecule immersed in a low *De* (<0.3) flow must adopt a sequence of configurations that admit passage through the narrow waist region of an adjacent constriction. For $d = 7\ \mu$m, the cross-sectional dimension of such regions is about 1 μm, so passage for a flexible molecule with $R_g = 0.7\ \mu$m is not much impeded; the free energy barrier is of order kT or smaller, and thermal motions make crossings frequent even in the absence of flow. Nonetheless, because of the configurational hindrances, the average velocity of DNA through a particle bed is lower than for solvent. This mode of "entropic barriers" transport has been described previously in the context of electrophoretic migration of flexible polymers in gels at low applied electric field, and there is no reason to expect the process here to be fundamentally different. (Friction coefficients during constriction passage, however, may not be the same for the two experiments.) At lower values of R_g/d ($\ll 1$) than examined, we hypothesizes a crossover to transport by the hydrodynamic chromatography mechanism, the order of DNA and solvent migration rates thereby inverted due to the diminished influence of constrictions and the increased impact of velocity gradients. Unfortunately, we were unable to obtain average DNA velocity data for $De < 0.25$, largely because at this limit the molecules move almost as frequently in and out of the focal plane as they move in the flow direction, making single molecule tracking problematical. It is expected that, for R_g/d of order-of-magnitude unity, as in the current experiment, the normalized DNA velocity in low *De* flows will map directly onto the normalized hindered diffusion coefficient or normalized mobility.[36–39]

Above the first *De* transition, the converging flow between bed spheres is strong enough to deform passing λ-DNA to molecular strains of order unity, thereby reducing the effective barrier height assigned to a constriction; flow-induced stretching allows better conformational accommodation of a DNA molecule. The reduced barrier height raises normalized velocity compared to that of the low *De* regime. In both regimes, however, since barrier height dominates, average DNA velocity remains lower than the average fluid velocity. When the molecular strain accumulated during one constriction passage can relax during a molecule's residence in the next void, as noted experimentally, chain extension remains small. We term the dynamics across this intermediate regime as "flow-perturbed entropic barriers transport".

In the high *De* regime ($De > 1.0$), dynamics are much more complex. At the heart of the complexity are "entanglements" formed by DNA molecules as they wrap around the contact point between two touching bed particles. Such entanglements never form in the low and moderate *De* regimes, but they are frequent across the entire high *De* regime. We postulate that fluctuating chain elongations at intermediate *De* grow with this parameter, creating maximum chain dimensions comparable to *d* finally at $De = 1$, an event that, by enabling effective entanglement at contact points, triggers an abrupt *De* transition. Less stretched chains apparently can slide around the contact points so readily that entanglements are too transient to observe.

Once a chain is entangled, its two free sections are quickly dragged by flow downfield, creating "U"- and "J"-shaped configurations with typical dimensions in the flow direction much larger than *d*. Disentanglement by flow-induced sliding over the contact point eventually releases the molecule, the longer of the two elongated chain sections nearly always winning the "tug of war" at the contact point. The time to disengage is characteristically longer than the time for chains to unravel in flow, making substantial stretching almost continuous, both during entanglement and afterward. Importantly, we observe that recently released molecules move much faster than the average solvent velocity. The reason for their high speed is unclear; possibly the tension exerted on aligned molecules keeps them strongly positioned along central streamlines (away from bed particle surfaces), where the local solvent velocity is much above the average solvent velocity. Experiments show that cycles of stationary entanglement and fast motion alternate so that the time-averaged normalized average axial velocity is much higher than for the fluid.

Entanglements initiate in two distinct manners. In one, a single small kink abruptly appears along a previously flow-aligned DNA chain (i.e., one adopting a zigzag conformation oriented in the flow direction). The chain then folds at the kink, which is pinned, forming a "U"- or "J"-shaped configuration as the upstream chain section sweeps past the kink. In the second, leading segments of a flow-aligned chain abruptly stop moving as a result of what appears to be a head-on collision with a bed particle, After a lull in which the chain convectively collects its collapsing tail, two chain arms rapidly propagate downfield, usually forming a "U"- or "J"-shaped configuration. If propagation occurs before the tail is fully collected, a short-lived "Y"-shaped conformation develops. The head-on entangle-

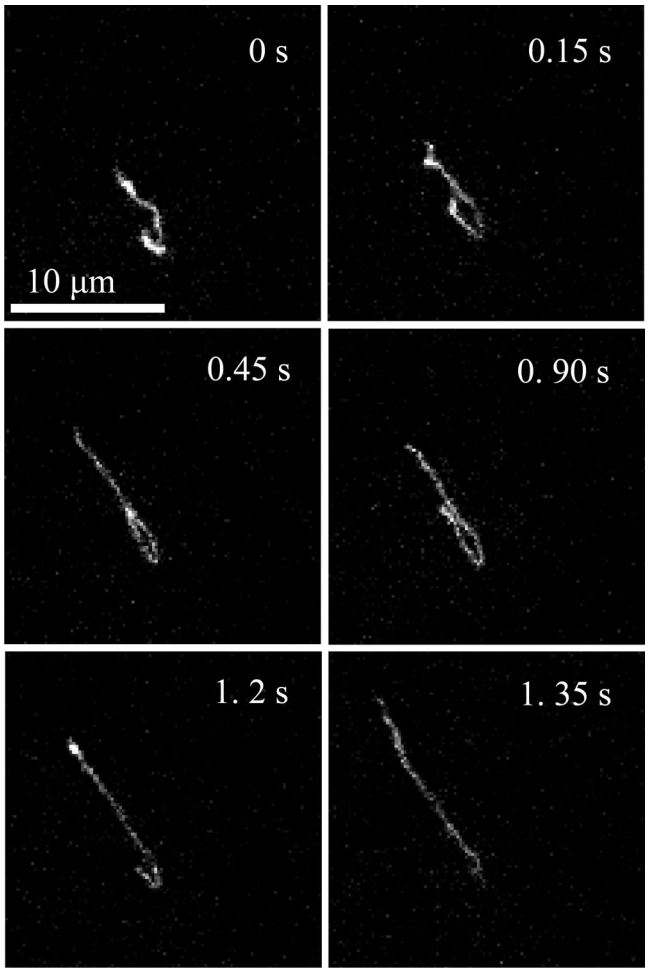

Figure 8. Entanglement and relaxation of λ-DNA in a bed of 1.3 μm particles. Note "J"-shaped conformations at intermediate times.

ment process is the most prevalent.

Figure 8 shows the progression of conformations for a single DNA molecule during and after entanglement. In this instance, high *De* flow was imposed in a bed of smaller latex particles ($d = 1.3$ μm), which more effectively create entanglements. The rapidly formed "J"-shaped configuration of the figure's first image (initiated from the unentangled chain in less than 0.3 s) took about 1.35 s to release, and at release, the chain was almost fully extended, as seen in the last image. The chain then maintained the same basic linear conformation, albeit with local flexing about particles, as it moved downfield, eventually entangling again ~0.5 s later (not shown). Higher *De* flow is easier to create at smaller d, but unfortunately, flow rate at $d = 1.3$ μm proved impossible to measure by the tracer method; from the observed migration rate of unentangled DNA, we estimate that *De* is 20−30 for the images of Figure 8. At such high *De*, two additional features emerge with the smaller bed particles. First, chains in fully stretched conformations occasionally undergo flow-induced cleavage somewhere in their more taut midsection, the resulting two fragments recoiling away from the break site. Such fragments, perhaps because of their lower extension, migrate visibly more slowly than unbroken chains, revealing that migration rate at high *De* is strongly chain length dependent. Second, as seen in the middle conformation of Figure 9, interior herniated regions can stretch downfield when a chain is entangled at two locations. As also shown, the same chain at earlier time transiently displayed a "Y"-shaped conformation due to head-on collision.

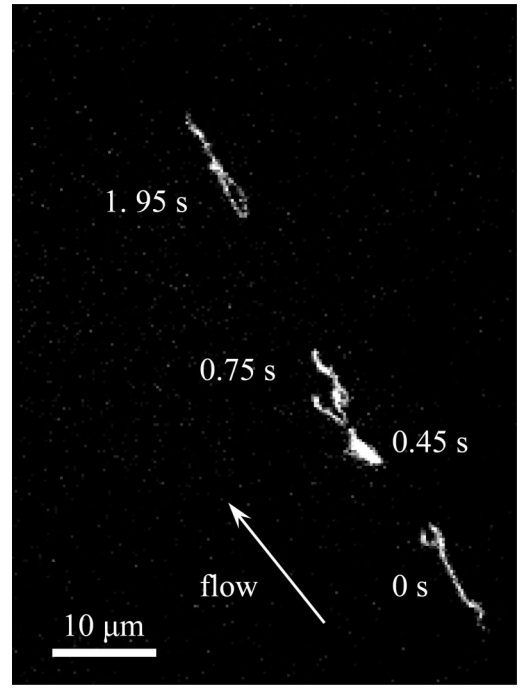

Figure 9. Trajectory of λ-DNA in a bed of 1.3 μm particles. Note "Y" conformation at 0 s and double entanglement at 0.75 s.

Relevance/Comparison of Visualized Conformations. The chain dynamics visualized in this study bear similarities to those visualized during gel electrophoresis, and in particular, as the driving field of either experiment increases, many of the same conformations are observed. Strong nonuniformity of the applied velocity field in a particle bed, as opposed to near uniformity of the apparently electric field in a gel, apparently has little impact on chain conformation and velocity so long as chain and pore have comparable dimensions. However, chain dynamics of the two experiments are not entirely the same. The intermediate *De* regime of the flow experiment, with its limited chain extension, is not seen in gel electrophoresis. Also, prevalence of head-on collisions leading to entanglement seems specific to the flow experiment. For entangled chains in both experiments, stretched "U"- and "J"-shaped conformations are seen at high field, and stretched conformations relax indistinguishably. We attribute the dynamical distinctions between the two environments mainly to the differences in pore geometry. For gel electrophoresis, a relatively open pore space is intersected by fibril-like obstacles, each with a diameter much smaller than the R_g, while for our flow experiment, polymers must squeeze through pore openings framed by compact obstacles (i.e., bed particles) large compared to R_g. Chains at high driving field in the flow experiment thereby undergo frequent head-on collision and, when strongly stretched and oriented, assume zigzag conformations susceptible to kinking. Dynamical differences are accentuated at higher d/R_g, which forces larger lateral excursions by polymers to avoid bed particles. We are unaware of observations of field-induced chain scission during gel electrophoresis, but at higher field strengths, relatively faster migration by longer chains is well-known.

A key objective of this study was elucidation of the molecular mechanisms for MTF, typically undertaken at $d/R_g \sim 10-20$, a ratio mimicked by us through selection of λ-DNA and bed particles of appropriate diameter. Although geometrically similar, our size scale is about 10 times that of MTF to facilitate optical imaging. Despite significant effort, we were unable to track DNA conformation and velocity in the *De* range relevant to MTF, typically 0.001−0.1. In MTF, starting at $De \sim 0.01$, polymer migration rate increases with increasing average solvent

velocity; while we also see a migration rate increase, it triggers at a much higher *De*.

Conclusion

Flexible polymers in dilute solution were visualized by fluorescence microscopy during their pressure-driven convection through a packed bed of small, micron-sized spheres, environments and conditions akin to those of polymer chromatography experiments. After abandoning closed channels flow devices because of incompatibility between high-pressure drop and microscopic imaging, wicking was chosen to drive fluid motion in an open channel microfluidic device. By proper choice of imaging optics, observations could be performed on labeled λ-DNA ($R_g = 0.7\ \mu$m) well away from the region of perturbed flow at the bed boundary. Individual chain dynamics could be tracked at the size scale of a single bed particle with more-than-adequate spatial and time resolution. For $d/R_g \sim 1-10$, characteristic conformational transitions were detected at two well-defined values of *De*: one at $De \sim 0.3$ and the second at $De \sim 1.0$. The latter transition is associated with onset of entanglement by a single chain with sphere contact points; such entanglements have similar dynamics to those previously visualized in gel electrophoresis. At lower *De*, polymers migrate by entropic barriers-mediated motion ($De < 0.3$) or flow-perturbed entropic barriers-mediated motion ($0.3 < De < 1.0$); because of the conformational constraints of bed constrictions, average migration rate at low *De* is slower than for solvent. Surprisingly, in the higher *De* regime, average migration rate is faster than for solvent even though chains are immobilized by entanglement at most times.

Experiments probing the full parameter space of d/R_g and *De* are planned. One key objective is to probe chain dynamics at even lower *De*, bringing visualization conditions closer to those of MTF and related forms of polymer chromatography. Unfortunately, increasing out-of-focal plane motions make time-dependent imaging difficult at $De < 0.25$. Trends for polymer migration rate found by this study, when assessed alongside migration behaviors determined previously by chromatography, suggest a complex array of conformational dynamics across the d/R_g-De parameter space even in this seemingly simple environment of impenetrable, nearly monodisperse packed spheres. Understanding polymer-flow-confinement interactions for pressure-driven flows is an essential first step in developing microfluidic separation devices for uncharged polymers. Only with this understanding in-hand can microscopic confinement geometry and flow conditions be optimized to afford the greatest discrimination by molecular architecture or molecular weight.

Acknowledgment. The Dow Chemical Company provided financial support for this project, and Patrick Smith and David Meunier, both of Dow, generously offered their advice throughout, as did M. Muthukumar (University of Massachusetts Amherst). Much of the research was conducted in the shared optical microscopy facility of The University of Massachusetts MRSEC in Polymers, funded by the NSF.

References and Notes

(1) Lathe, G. H.; Ruthven, C. R. J. *Biochem. J.* **1956**, *62* (4), 665–674.
(2) Porath, J.; Flodin, P. *Nature (London)* **1959**, *183* (4676), 1657–1659.
(3) Lecourtier, J.; Chauveteau, G. *Macromolecules* **1984**, *17* (7), 1340–1343.
(4) Hoagland, D. A.; Prudhomme, R. K. *J. Appl. Polym. Sci.* **1988**, *36* (4), 935–955.
(5) Hirabayashi, J.; Kasai, K. I. *Anal. Biochem.* **1989**, *178* (2), 336–341.
(6) Hirabayashi, J.; Ito, N.; Noguchi, K.; Kasai, K. *Biochemistry* **1990**, *29* (41), 9515–9521.
(7) Marshall, R. J.; Metzner, A. B. *Ind. Eng. Chem. Fundam.* **1967**, *6* (3), 393–000.
(8) Smith, S. B.; Aldridge, P. K.; Callis, J. B. *Science* **1989**, *243* (4888), 203–206.
(9) Schwartz, D. C.; Koval, M. *Nature (London)* **1989**, *338* (6215), 520–522.
(10) Meunier, D. M.; Smith, P. B.; Baker, S. A. *Macromolecules* **2005**, *38* (12), 5313–5320.
(11) Perkins, T. T.; Smith, D. E.; Chu, S. *Science* **1997**, *276* (5321), 2016–2021.
(12) Keller, A.; Odell, J. A. *Colloid Polym. Sci.* **1985**, *263* (3), 181–201.
(13) Smith, D. E.; Babcock, H. P.; Chu, S. *Science* **1999**, *283* (5408), 1724–1727.
(14) Babcock, H. P.; Teixeira, R. E.; Hur, J. S.; Shaqfeh, E. S. G.; Chu, S. *Macromolecules* **2003**, *36* (12), 4544–4548.
(15) Fang, L.; Hu, H.; Larson, R. G. *J. Rheol.* **2005**, *49* (1), 127–138.
(16) Teclemariam, N. P.; Beck, V. A.; Shaqfeh, E. S. G.; Muller, S. J. *Macromolecules* **2007**, *40* (10), 3848–3859.
(17) Haas, R.; Durst, F. *Rheol. Acta* **1982**, *21* (4−5), 566–571.
(18) Durst, F.; Haas, R.; Interthal, W. *J. Non-Newtonian Fluid Mech.* **1987**, *22* (2), 169–189.
(19) Zimm, B. H. *J. Chem. Phys.* **1956**, *24* (2), 269–278.
(20) Han, J.; Craighead, H. G. *Science* **2000**, *288* (5468), 1026–1029.
(21) Zhang, H.; Wirth, M. J. *Anal. Chem.* **2005**, *77* (5), 1237–1242.
(22) Bakajin, O. B.; Duke, T. A. J.; Chou, C. F.; Chan, S. S.; Austin, R. H.; Cox, E. C. *Phys. Rev. Lett.* **1998**, *80* (12), 2737–2740.
(23) Huang, L. R.; Tegenfeldt, J. O.; Kraeft, J. J.; Sturm, J. C.; Austin, R. H.; Cox, E. C. *Nat. Biotechnol.* **2002**, *20* (10), 1048–1051.
(24) Doyle, P. S.; Bibette, J.; Bancaud, A.; Viovy, J. L. *Science* **2002**, *295* (5563), 2237–2237.
(25) Volkmuth, W. D.; Austin, R. H. *Nature (London)* **1992**, *358* (6387), 600–602.
(26) Minc, N.; Futterer, C.; Dorfman, K.; Bancaud, A.; Gosse, C.; Goubault, C.; Viovy, J. L. *Anal. Chem.* **2004**, *76* (13), 3770–3776.
(27) Kaji, N.; Tezuka, Y.; Takamura, Y.; Ueda, M.; Nishimoto, T.; Nakanishi, H.; Horiike, Y.; Baba, Y. *Anal. Chem.* **2004**, *76* (1), 15–22.
(28) Randall, G. C.; Doyle, P. S. *Macromolecules* **2005**, *38* (6), 2410–2418.
(29) Randall, G. C.; Doyle, P. S. *Macromolecules* **2006**, *39* (22), 7734–7745.
(30) Hoagland, D. A.; Arvanitidou, E.; Welch, C. *Macromolecules* **1999**, *32* (19), 6180–6190.
(31) Liu, Y. G.; Radke, W.; Pasch, H. *Macromolecules* **2005**, *38* (17), 7476–7484.
(32) Liu, Y. G.; Radke, W.; Pasch, H. *Macromolecules* **2006**, *39* (5), 2004–2006.
(33) Washburn, E. W. *Phys. Rev.* **1921**, *17* (3), 273–283.
(34) Liu, Y. G.; Jun, Y. G.; Steinberg, V. *Macromolecules* **2007**, *40* (6), 2172–2176.
(35) Smith, D. E.; Perkins, T. T.; Chu, S. *Macromolecules* **1996**, *29* (4), 1372–1373.
(36) Arvanitidou, E.; Hoagland, D. *Phys. Rev. Lett.* **1991**, *67* (11), 1464–1466.
(37) Hoagland, D. A.; Muthukumar, M. *Macromolecules* **1992**, *25* (24), 6696–6698.
(38) Muthukumar, M.; Baumgartner, A. *Macromolecules* **1989**, *22* (4), 1937–1941.
(39) Nykypanchuk, D.; Strey, H. H.; Hoagland, D. A. *Science* **2002**, *297* (5583), 987–990.

MA800430A